Large critical current densities and pinning forces in CSD-grown superconducting $GdBa_2Cu_3O_{7-x}$ -$BaHfO_3$ nanocomposite films

Large critical current densities and pinning forces in CSD-grown superconducting GdBa$_2$Cu$_3$O$_{7-x}$-BaHfO$_3$ nanocomposite films

Pablo Cayado, **Manuela Erbe, Sandra Kauffmann-Weiss, Carl Bühler, Alexandra Jung, Jens Hänisch and Bernhard Holzapfel**

Karlsruhe Institute of Technology (KIT), Institute for Technical Physics (ITEP), Hermann von Helmholtz Platz 1, D 76344 Eggenstein Leopoldshafen, Germany

E mail: pablo.cayado@kit.edu

Abstract

GdBa$_2$Cu$_3$O$_{7-x}$-BaHfO$_3$ (GdBCO-BHO) nanocomposite (NC) films containing 12 mol% BHO nanoparticles were prepared by chemical solution deposition (CSD) following the TFA route on SrTiO$_3$ (STO) single crystals and buffered metallic tapes supplied by two different companies: Deutsche Nanoschicht GmbH and SuperOx. We optimized the preparation of our GdBCO-BHO solutions with acetylacetone making the film synthesis very robust and reproducible, and obtained 220 nm films with excellent superconducting properties. We show the structural, morphological and superconducting properties of the films after a careful optimization of the processing parameters (growth temperature, oxygen partial pressure and heating ramp). The films reach critical temperatures (T_c) of ∼94 K, self-field critical current densities (J_c) of >7 MA cm^{-2} and maximum pinning force densities (F_p) of ∼16 GN m^{-3} at 77 K on STO and T_c of ∼94.5 K and J_c > 1.5 MA cm^{-2} on buffered metallic tapes. The transport properties under applied magnetic fields are significantly improved with respect to the pristine GdBCO films. The GdBCO-BHO NC films on STO present epitaxial c-axis orientation with excellent out-of-plane and in-plane texture. The films are, in general, very dense with a low amount of pores and only superficial indentations. On the other hand, we present, for the first time, a systematic study of CSD-grown GdBCO-BHO NC films on buffered metallic tapes. We have used the optimized growth conditions for STO as a reference and identified some limitations on the film synthesis that should be overcome for further improvement of the films' superconducting properties.

Keywords: CSD, TFA route, GdBCO, nanocomposites, buffered metallic tapes, BHO

(Some figures may appear in colour only in the online journal)

1. Introduction

One of the most active topics in the field of applied super-conductivity is the fabrication of second-generation super-conducting tapes, called Coated Conductors (CCs). Those tapes have a multilayer structure consisting of a metallic substrate, buffer layers, the superconducting film and capping layers [1 3]. From the first-generation tapes, they do not only differ in the type of the high-temperature superconductor (HTS) material but also in the fabrication method. The first-generation tapes are prepared by the powder-in-tube (PIT)

technique and are based on Bi$_2$Sr$_2$Ca$_{n-1}$Cu$_n$O$_{2n+4+x}$ (BSCCO) as HTS material, while in the case of the CCs, REBa$_2$Cu$_3$O$_{7-x}$ (REBCO, RE rare earth) compounds are used for which the PIT technique is not applicable [4 6]. However, it is still under debate which REBCO compounds are most adequate for each application due to the necessity to accomplish certain requirements at different temperature and magnetic field ranges.

Historically, most of the studies were focused on YBa$_2$Cu$_3$O$_{7-x}$ (YBCO or Y-123 phase), since it was the first REBCO compound discovered with a critical temperature (T_c)

higher than liquid nitrogen temperature (77 K) and it is relatively easily prepared as bulk or thin film. Yet, there are other *RE*BCO compounds that could exhibit better properties, as it has already been proven in the past [7–9]. Those differences in the superconducting properties arise from the variations in the electronic structures, valence states and, largely, the ionic radii of the *RE* atoms within the structures [10–13]. Their sizes determine the distances between different planes within the structure and, therefore, the interaction between the orbitals of different atoms which leads to a change in properties of the different compounds. Despite the fact that some of these *RE*BCO compounds present better performances than YBCO, they are often more difficult to synthesize and, therefore, not as often used as YBCO. These difficulties are mostly related to the partial substitution of the Ba^{2+} sites by large *RE* ions and the low stability of the 123 phase in some of the *RE*BCO compounds [7, 10, 14, 15]. In the case of small *RE* ions such as Yb^{3+} and Lu^{3+}, the formation of single-phase *RE*BCO is impeded, because the ions do not fit properly in the according lattice site, and thus, it is likely that vacancies on *RE* sites exist [10, 15].

One of the *RE*BCO compounds with a better performance than YBCO is GdBCO. This compound presents T_c values up to 95 K in bulk samples, single crystals and thin films [7, 16, 17]. This higher T_c value by roughly 3 K is linked with a shift of the irreversibility line towards higher *B* and *T*, which leads to an improvement of the in-field properties of GdBCO with respect to YBCO. In the past, GdBCO thin films were mainly prepared by *in situ* methods (where *in situ* refers to the crystallization of the superconducting phase): sputtering, pulsed laser deposition (PLD) or metal-organic chemical vapor deposition (MOCVD) [18–22]. However, in the search for a scalable and low-cost technique for the preparation of CCs, some researchers have focused on the chemical solution deposition (CSD) as an attractive option for thin film growth [23–26]. In general, most of this work followed the well-known TFA-MOD-route [27]. This route has already shown promising properties for GdBCO films [17, 28–33], but still the effort is not comparable to YBCO and so there is room for improvement, as we will demonstrate in this work.

In order to improve the in-field performance, we introduced secondary phases in our films creating GdBCO nanocomposites (NCs). The insertion of different secondary phases for preparing NCs has been extensively investigated by many groups showing that the in-field properties of *RE*BCO films can be vastly improved by both the '*in situ*' and the '*ex situ*' approaches [34–39]. We have opted for the '*in situ*' approach, in which the nanoparticles (NPs) are spontaneously segregated in the superconductor matrix during the growth process, to include $BaHfO_3$ (BHO) NPs in GdBCO films, a strategy that has already shown excellent results in former works reported by our group [36].

We have also transferred our solution to buffered metallic tapes. This is the final step at the lab scale before going to long-length production. Previous studies with GdBCO or GdBCO NCs deposited on buffered metallic tapes focused on physical deposition techniques such as reactive co-evaporation by deposition and reaction [40–42] and PLD [43–46]. In contrast, CSD-grown GdBCO films on tapes have not been investigated, to our knowledge, before this study.

2. Sample preparation and characterization techniques

2.1. Synthesis of the precursor solutions

The method for the preparation of the TFA solution is based on the one proposed by Erbe *et al* [30, 36]. The pristine solutions (the ones that contain no secondary phases) are made by mixing Gd, Ba and Cu acetates (purity > 99.99%, Alfa Aesar) weighed out to give a stoichiometric 1:2:3 ratio of the metal cations in deionized water. Then, an excess of trifluoroacetic acid (TFAH, 99.5+%, Alfa Aesar) is added to convert the acetates into trifluoroacetates. The remaining water and other impurities are eliminated by a rotary evaporator obtaining a highly viscous residue that is re-diluted in absolute methanol (99.9%). In order to further reduce the undesired remaining water, methanol is evaporated again several times in vacuum. The final concentration of $0.25\,mol\,l^{-1}$ in gadolinium is adjusted with anhydrous methanol ending with a dark blue solution.

In the case of BHO-containing solutions, the procedure is slightly changed from the previous works: the addition of the required amount of hafnium(IV) 2, 4-pentanedionate ($Hf(acac)_4$) (97+%, Alfa Aesar) is not made at the end of the process, but instead mixed with the other precursor salts to achieve a 12 mol% BHO ('12%BHO' from now) concentration in the final films with regard to *RE*. This modified procedure increases the control and the flexibility of the solution preparation and opens the possibility for future investigations to increase the final concentration of BHO in the solution that, in the other case, is limited to 12–13 mol% due to solubility limitations of the $Hf(acac)_4$ in the final solution.

2.2. Thin film preparation

The 220 nm GdBCO + 12%BHO films studied in this work were prepared, firstly, by depositing the precursor solutions on $10\,mm \times 10\,mm$ (100) oriented $SrTiO_3$ (STO) single crystals or biaxially textured buffered metallic tapes ('tapes' from now) via spin coating (6000 rpm for 30 s for the STO and 5000 rpm for 30 s for the tapes). The subsequent 'standard' pyrolysis and growth processes are described in [30]. The modifications to the 'standard' growth process that lead to the presented results will be discussed in depth later.

2.3. Thin film characterization

The properties of the solutions used in this work were analyzed by infrared (IR) spectroscopy on a Vertex 70 ATR IR-spectrometer (*Bruker*). The microstructure and phase purity of the films were investigated by x-ray diffraction (XRD) using a *Bruker* D8 diffractometer with CuKα radiation. The surface morphology and cross-sections of the films after pyrolysis and growth were analyzed by a LEO 1530 scanning electron microscope (SEM) with field emission gun by *Zeiss*. Cross-sections
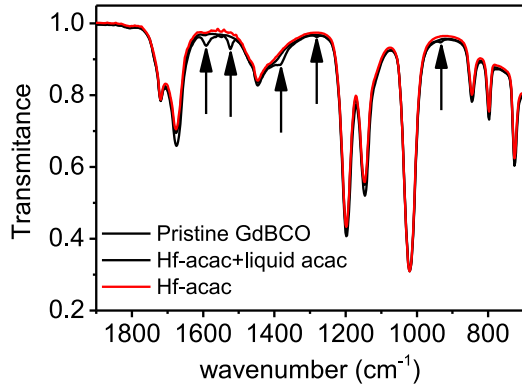
Figure 1. IR spectra of the pristine GdBCO and GdBCO + 12% BHO solutions with different amounts of acac. Only the solution with liquid acac additions shows additional bands marked by black arrows, which can be attributed to the presence of acac.

were prepared by an Ar-ion cross-section polisher IB-19500CP from *JEOL*. The field penetration was qualitatively investigated by magneto-optical imaging using an *Evico Magnetics* microscope. Self-field J_c at 77.6 K, J_c^{sf}, was measured inductively with a Cryoscan (*Theva*, 50 μV criterion), and T_c ($T_{c,90}$, i.e., the temperature at which the resistance is 90% of the value above the transition), ΔT_c ($T_{c,90}$ $T_{c,10}$), $J_c(B)$ (1 μV cm^{-1} criterion of transport J_c) and the J_c anisotropy of the films were studied with a 14-T *Quantum Design* Physical Property Measurement System. The measurements were done on 10 20 μm tracks prepared by a photolithography process and wet-chemical etching.

3. Results and discussion

3.1. Solution characterization

A thorough investigation of pristine *RE*BCO solutions and the role of acetylacetone (2, 4-pentanedione, 'acac' from now) as a solution additive was carried out previously and can be found in [30]. The conclusion was that acac coordinates at the Cu cations, which causes a color change from dark blue to dark green. Once the pristine GdBCO solution was prepared, this color change was similarly observed when Hf(acac)$_4$ was added to create the GdBCO + BHO solution [36]. However, with the new solution preparation method used in this work, the finally adjusted solutions have the same dark blue color as the hafnium free solutions, even with Hf(acac)$_4$ already inside. This indicates that the acac from the Hf precursor is removed during the purification process. Therefore, as a final step, liquid acac (2, 4-pentanedione, Alfa Aesar, 99%) is added to the solution in a final molar ratio of $\sim$35% acac/*RE*, which is similar to the amount reached when the acac comes from the Hf precursor. Again, this addition changes the color of the solution from a dark blue to a dark green color and has an important impact on the performance of the films as demonstrated in previous works [30].

In order to prove that acac is removed during the successive evaporation steps in the rotary evaporator, we have investigated several solutions by IR spectroscopy. Figure 1

compares the IR spectra of three solutions: pristine GdBCO (black), GdBCO + 12%BHO with Hf(acac)$_4$ added in the beginning but without any liquid acac addition (Hf-acac, red), and the solution used for preparing the films in this work, GdBCO + 12% BHO with Hf(acac)$_4$ added in the beginning as well as liquid acac added as a final step to reach a molar ratio of $\sim$35% acac/*RE* (Hf-acac+liquid acac, blue).

Whereas the solutions of pristine GdBCO and GdBCO with Hf(acac)$_4$ show very similar IR spectra, the spectrum of the GdBCO Hf-acac+liquid acac solution shows additional bands (black arrows). This means, firstly, that these bands are caused by the presence of acac in the solution and secondly that the acac that is introduced in the solution by the addition of the initial Hf(acac)$_4$ salt is removed during the solution preparation. Thus, with the new solution preparation method our only source of acac is the liquid acac added as a final step. So it is important to include this final addition of liquid acac to still benefit from acac improvement in the final quality of the films. The exact compounds that cause the extra bands in the IR spectrum are unknown and under current investigation.

3.2. Optimization of growth processing parameters on STO

As mentioned, we have changed the solution preparation method. This makes an optimization of the processing parameters of the film growth for these new solutions necessary.

3.2.1. Heating ramp.
The heating ramp used during the growth process to reach the final crystallization temperature can have great importance for the final properties of the films as it can influence the nucleation of the *RE*BCO grains. Some studies report optimized heating ramps in the range of 20 25 °C min^{-1} for pristine YBCO and YBCO NC films [24, 25, 47]. For GdBCO films, there is not much information available. Therefore, we have investigated the evolution of the structural and superconducting properties of GdBCO + 12%BHO films using heating ramps between 10 and 85 °C min^{-1} during the growth process. These results are compared with YBCO + 12% BHO films prepared in a similar way. For the growth of the GdBCO + 12%BHO films we have maintained a growth (or crystallization) temperature, T_{growth}, of 810 °C with an oxygen partial pressure, $p(O_2)$, of 100 ppm. The YBCO + 12%BHO films were grown at 770 °C with a $p(O_2)$ of 200 ppm.

The XRD patterns of the YBCO + 12%BHO and GdBCO + 12%BHO films grown at different heating ramps are compared in figure 2. The diffraction patterns of the YBCO + 12%BHO films are all very similar, showing only the reflections of (00*l*)YBCO as well as the substrate reflections and signs of BHO. However, in the case of the GdBCO + 12%BHO films, there is a clear influence of the heating ramp on the structure of the films. By the use of slow ramps (10 or 20 °C min^{-1}), the formation of misoriented grains, as visible by an intense (103)GdBCO reflection, and *a b* grains ((200)GdBCO and (300)GdBCO) is promoted, If the heating ramp is increased to 85 °C min^{-1}, highly (00*l*)-oriented GdBCO is formed. In all GdBCO + 12%BHO diffractograms, intermediate phases of the GdBCO formation
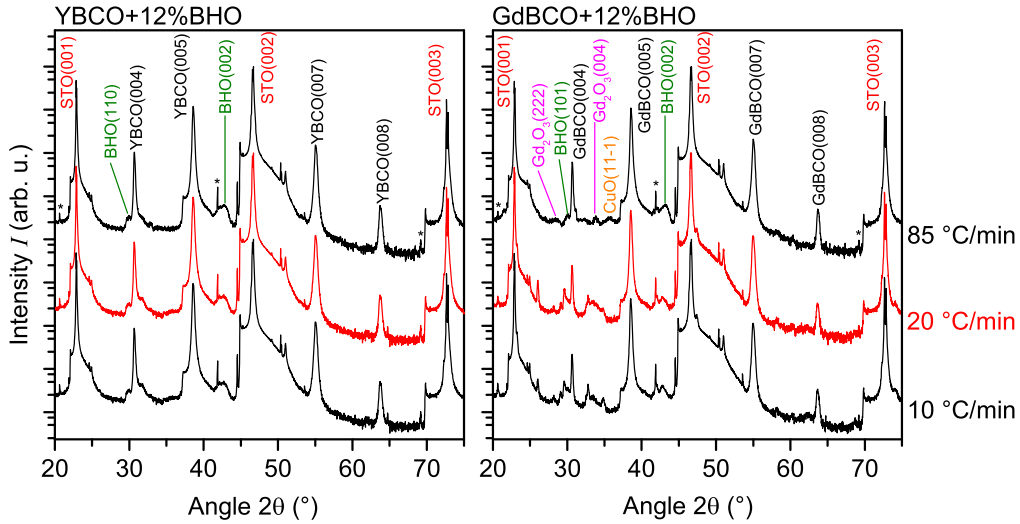
Figure 2. XRD spectra of (a) YBCO + 12%BHO films and (b) GdBCO + 12%BHO films grown with different heating ramps. Reflections indicated with * correspond to K_β reflections of STO.

reaction are visible, which means that the growth conditions chosen for the growth are not, yet, optimal.

The different influence of the heating ramp on both compounds can also be perceived in figure 3 where the superconducting properties are represented as a function of the heating ramp. While T_c of both compounds stays more or less constant, J_c^{sf} at 77.6 K behaves completely different. In the case of YBCO + 12%BHO, the values vary within a range of 1 MA cm^{-2} around 3.5 MA cm^{-2}. For GdBCO + 12%BHO they increase strongly from 0.5 MA cm^{-2} to 6.1 MA cm^{-2} with increasing heating ramp. This shows that the superconducting properties of the GdBCO + 12%BHO films strongly depend on the heating ramp. This is directly linked with the XRD patterns shown previously. The fact that the YBCO + 12%BHO films have similar patterns for all heating ramps without misoriented grains reflects in similar inductive J_c^{sf} values at 77.6 K. For GdBCO + 12%BHO films, the misoriented grains can only be avoided by a large heating ramp and therefore J_c^{sf} at 77.6 K shows a big improvement for the 85 °C min^{-1} heating ramp.

It is concluded that while the structure and superconducting properties of YBCO + 12%BHO films are not very sensitive to changes of the heating ramp, the structure and the superconducting properties of GdBCO + 12%BHO films depend heavily on the used heating ramp. A low heating ramp leads to the formation of misoriented and a-b grains which reduces drastically J_c. For this reason, the ramp of 85 °C min^{-1} was used for the rest of the experiments.

This different effect of the heating ramp on both kinds of films can be explained considering how the nucleation in REBCO films occurs. Focusing in the case of the heteronucleation, it is known that the c-axis nucleation is a favorable event only at low values of supersaturation. At high values of supersaturation, the probability of the c-axis, a-axis and random nucleation is similar because the energy barrier for each kind of nucleation becomes very similar. In general, the higher the temperature is, the lower the supersaturation (more specific details in [48]). Therefore, our aim
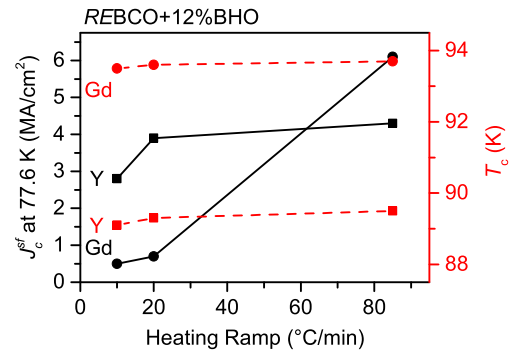
Figure 3. Dependence of the inductive J_c^{sf} at 77.6 K (black curves) and T_c (red curves) of 12% BHO containing YBCO (squares) and GdBCO (circles) nanocomposite films on the heating ramp during growth process.

with the fast heating ramp is to arrive as fast as possible at high temperatures to promote the c-axis nucleation and to avoid staying too long at lower temperatures which would promote a mixture of nucleation events. The differences in the structure and superconducting properties between YBCO + 12%BHO and GdBCO + 12%BHO films arise from the fact that the energy barrier for multiple nucleation events for GdBCO + 12%BHO films is lower than for YBCO + 12%BHO and, therefore, longer times at low temperatures will promote more misoriented or a-b grains in the case of GdBCO + 12%BHO films and, consequently, lower heating ramps are very detrimental in this case.

3.2.2. Oxygen partial pressure and growth temperature. The results above on varying the heating ramp have shown that by using a T_{growth} of 810 °C and a $p(O_2)$ of 100 ppm epitaxial GdBCO + 12%BHO films with $T_c = 93.7$ K and J_c^{sf} at 77.6 K $= 6.1$ MA cm^{-12} were achieved for optimal heating ramps. However, these films still contain some intermediate reaction phases (figure 2), that may worsen the superconducting properties. Thus, further optimization of T_{growth} and $p(O_2)$ may even lead to further enhancement of the superconducting
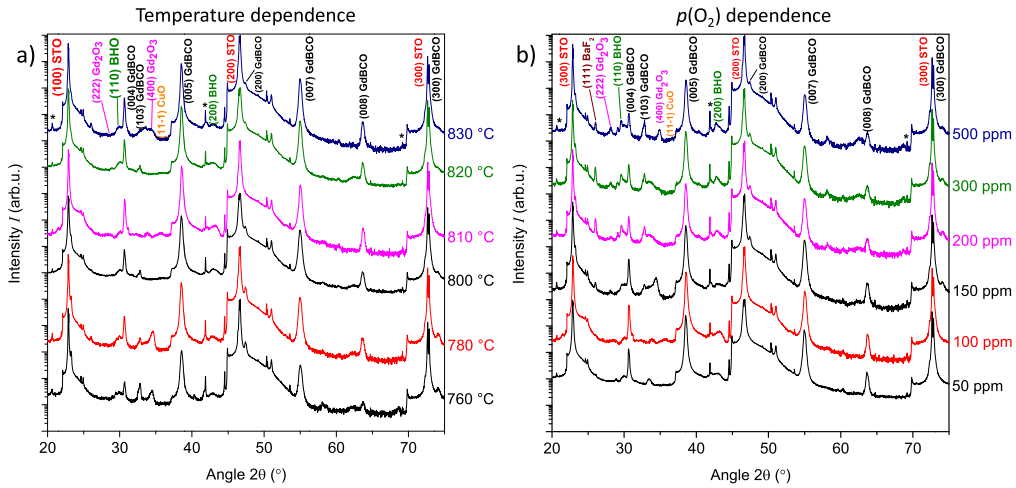
Figure 4. XRD patterns of GdBCO + 12%BHO films grown (a) at different T_{growth} with constant $p(O_2)$ (100 ppm) and (b) at different $p(O_2)$ with constant T_{growth} (810 °C). The diffractogram of 810 °C in (a) and 100 ppm in (b) represent the same film. Reflections indicated with * correspond to K_β reflections of STO.
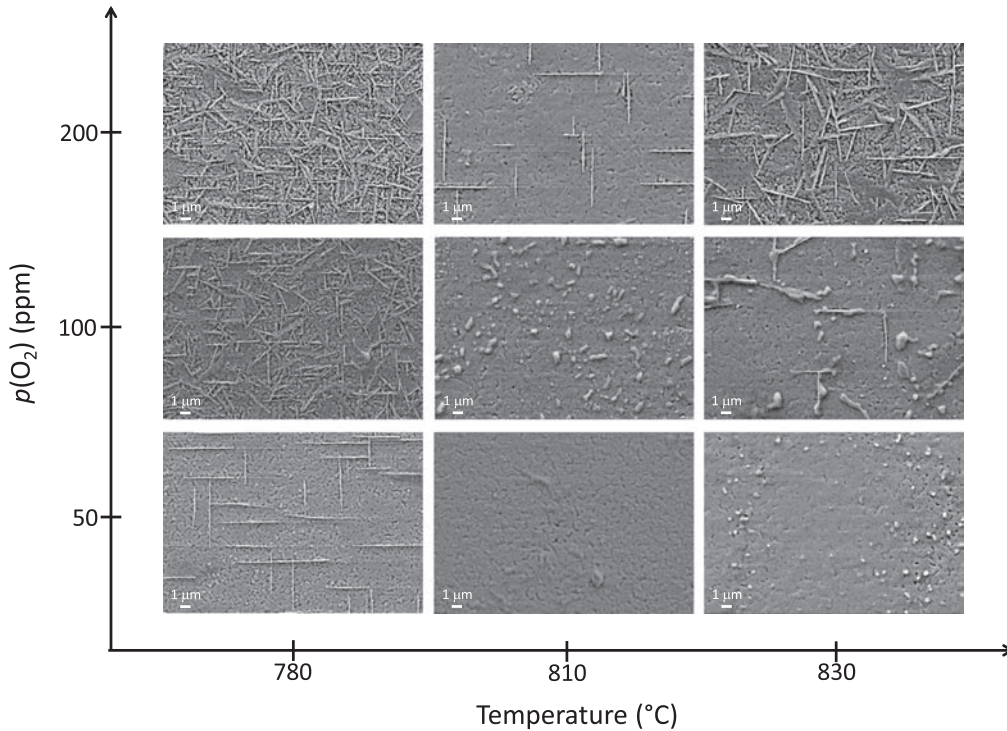
Figure 5. SEM pictures of GdBCO + 12%BHO films grown at different T_{growth} and $p(O_2)$.

properties. For this reason, we scanned a large range of the T_{growth} — $p(O_2)$ parameter space searching for the optimum set of parameters for maximizing T_c and J_c.

The optimum conditions of 810 °C and 50–100 ppm oxygen can be seen in XRD scans (figure 4), surface morphology (figure 5), and superconducting properties (figure 6). In the XRD patterns of several films grown at different temperatures but constant $p(O_2)$ of 100 ppm, (00*l*) GdBCO reflections can be seen for all T_{growth}. However, in most of the cases, this orientation coexists with misoriented grains resulting in a polycrystalline microstructure. Purely epitaxial growth is only achieved at 810 °C. The variation of

$p(O_2)$, figure 4(b)), manifests a similar situation. Polycrystalline growth is observed at high $p(O_2)$ (>100 ppm) and only by reducing $p(O_2)$ below 100 ppm purely epitaxial growth is achieved. The XRD patterns at 50 and 100 ppm are quite similar, with slightly more intermediate reaction phases visible for 100 ppm.

The dependence observed in XRD is confirmed by the SEM pictures in figure 5. Clearly, the areal density of *a–b* grains (white needle-shaped structures forming 90° between each other) and other misoriented grains (white needles oriented in any possible direction) increases at low T_{growth} and high values of $p(O_2)$. At high T_{growth} (>810 °C) and low
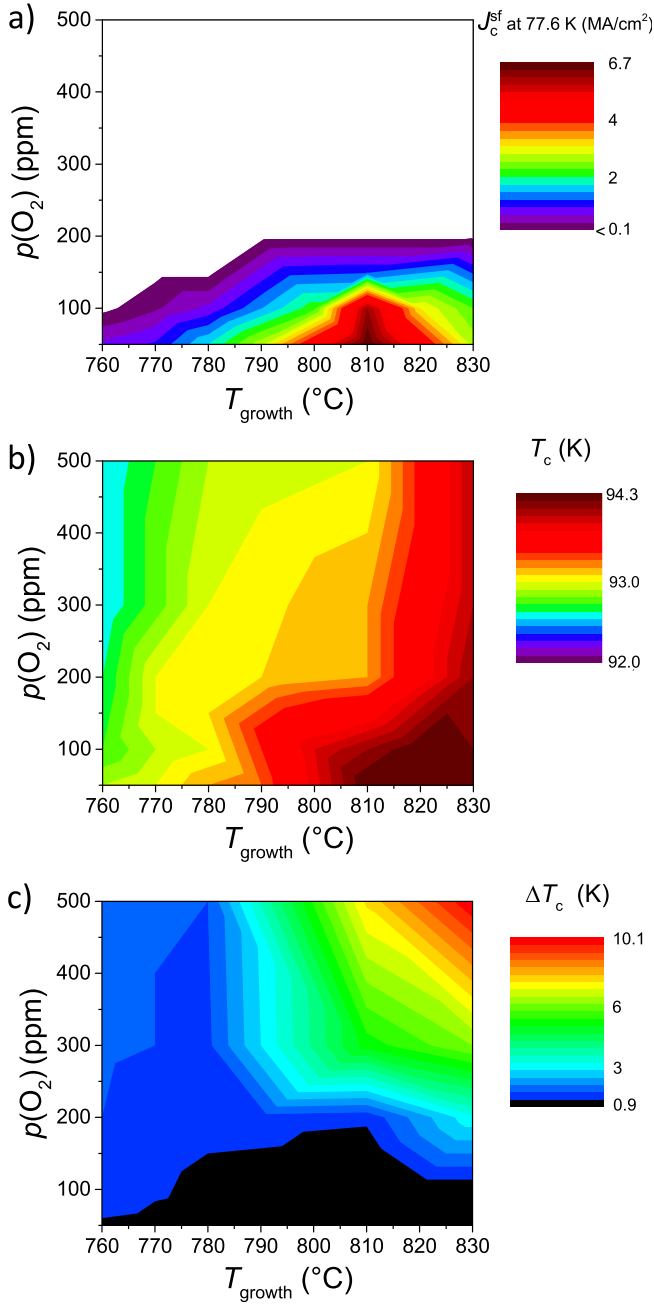
Figure 6. Dependence of (a) inductive J_c^{sf} at 77.6 K (white area means $J_c < 0.1$ MA cm^{-2}), (b) critical temperature T_c and (c) transition width ΔT_c of GdBCO + 12%BHO films for different T_{growth} and $p(O_2)$.

Figure 7. Left half of magneto optical images showing dendritic flux penetration at 16 mT of (a) a film grown at 810 °C and 100 ppm and (b) a sample grown under optimized conditions (810 °C and 50 ppm) at 16 mT.
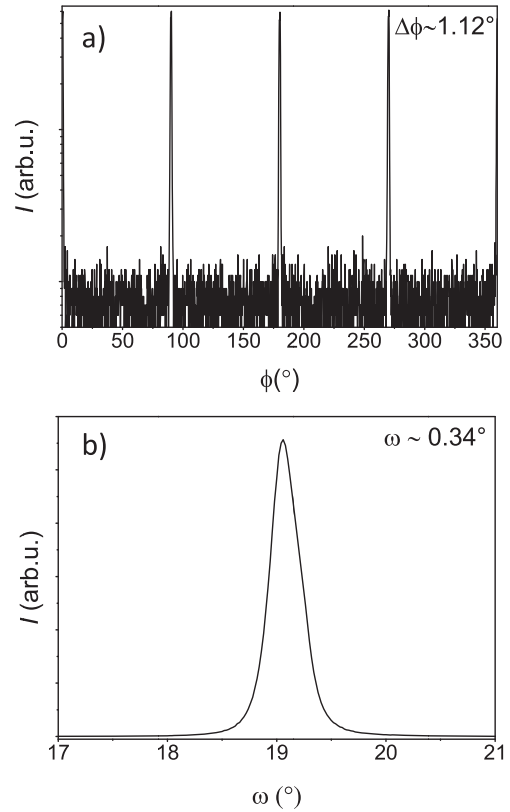
Figure 8. Texture measurements of an optimized GdBCO + 12% BHO film showing (a) the ϕ scan of (103)GdBCO and (b) the (005) GdBCO rocking curve.

values of $p(O_2)$ (<100 ppm) the films do not present any misoriented grains but the porosity increases slightly with respect to optimum temperature (810 °C). If we keep constant these high T_{growth} but increase the $p(O_2)$ above 100 ppm, a b or other misoriented grains appear again. Furthermore, the films grown at 810 °C and 50 and 100 ppm do not show a b grains at all. On the other hand, the porosity is very low for all the films and the films are very dense with only superficial indentations.

Finally, the superconducting properties of films grown at different temperatures and $p(O_2)$ are compared (figure 6).

Figure 6(a) indicates that the best values of J_c^{sf} at 77.6 K are achieved only in a very narrow region around 810 °C and between 50 and 100 ppm. Outside this region, the J_c values decrease very rapidly. The maximum J_c value is reached at 810 °C and 50 ppm of oxygen, conditions that correspond to purely epitaxial and very dense films. It is remarkable that, according to our results, the growth of GdBCO + 12%BHO
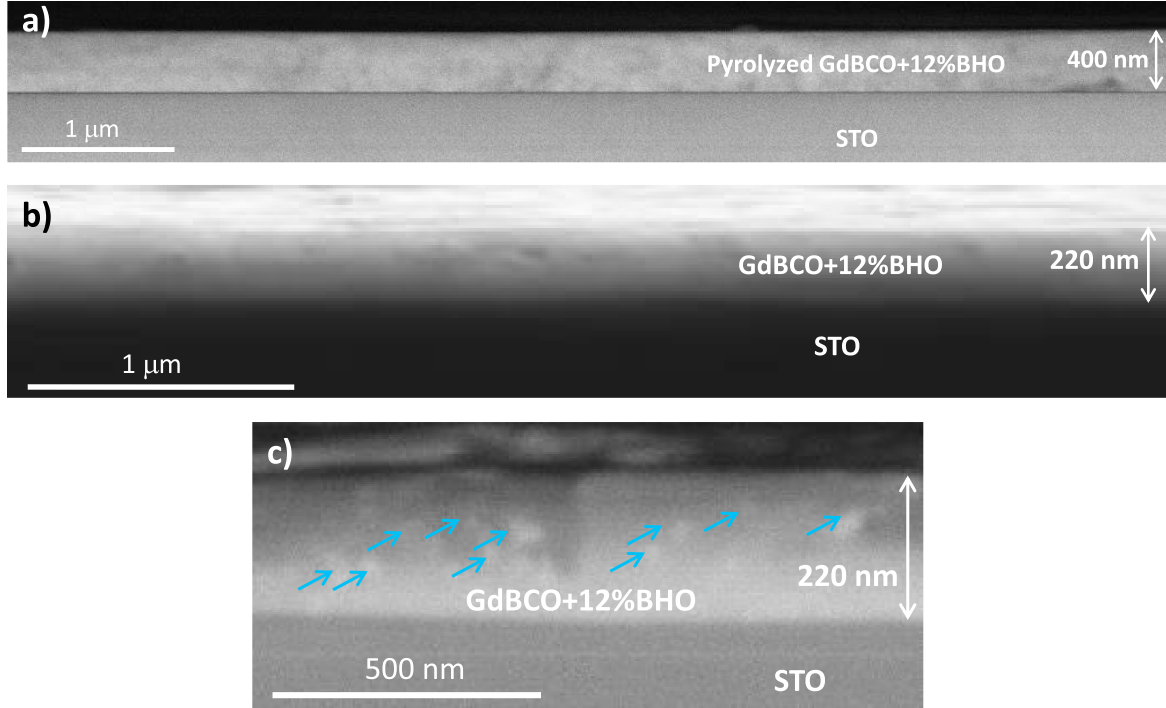
Figure 9. Cross section SEM images of (a) a pyrolyzed GdBCO + 12%BHO film taken on secondary electrons mode, (b) grown GdBCO + 12%BHO film taken on backscattered electrons mode and (c) zoom of image (b) showing the presence of BHO NPs (blue arrows). The GdBCO + 12%BHO film was prepared using the optimized conditions.

films should be carried out with $p(O_2) < 200$ ppm because in other cases the values of J_c^{sf} at 77.6 K are almost negligible. The window for optimal T_c, figures 6(b) and (c), is somewhat larger. The T_c values remain more or less constant with a variation of $\sim$2 K. The maximum values of around 94.3 K are reached at 810 °C 830 °C and 50 150 ppm. The lowest T_c values are found at low temperatures and high $p(O_2)$, where also the porosity is larger. The transition width ΔT_c, figures 6(c), is in the range of 1 K in most of the studied area, and only at high temperatures and high $p(O_2)$ the values deteriorate, indicating that the homogeneity of the films is degraded.

Regarding structure, surface morphology and super-conducting properties of the GdBCO + 12%BHO films, the best results are achieved at a $p(O_2)$ of 50 ppm, at much lower values than reported for YBCO films (always >150 ppm). This behavior is supported by the phase diagram of GdBCO, since the stability line is shifted towards higher temperatures and lower oxygen partial pressures with respect to YBCO allowing the growth at lower $p(O_2)$ [17, 49, 50]. The fact that the best properties are found at the lowest possible $p(O_2)$ with respect to the phase stability has been observed in YBCO films grown by the BaF_2 process previously [51] and has been explained as an effect of the large amount of oxygen vacancies on the oxygen sublattice at low partial pressures promoting cation diffusion and therefore structure ordering[51].

The field penetration behavior also depends strongly on the phase formation conditions even when the resulting J_c is very similar, as illustrated in magneto-optical images in figure 7. The figure compares (a) a film grown at 810 °C and 100 ppm and (b) a sample grown under optimized conditions

(810 °C and 50 ppm) with slightly higher J_c (figure 6(a)). Figures 7(a) and (b) depict how the flux penetrates both films when the field is set at 16 mT. Due to a higher J_c^{sf} (there is a difference of $\sim$1 MA cm^{-2} at 77.6 K between both films) the magnetic field penetrates the optimized film to a smaller depth (the black area of zero magnetic field is larger in the optimized film (b) than in film with lower J_c (a)). Similar features were observed in YBCO and YBCO NC films [52 54]. With these images we confirm the higher values of J_c in films grown at optimized conditions.

3.2.3. Measurements on optimized films. The GdBCO + 12% BHO films on STO for the analysis in the following section were grown at the optimum conditions: a heating ramp of 85 °C min^{-1}, a T_{growth} of 810 °C, and an oxygen partial pressure $p(O_2)$ of 50 ppm.

High-quality in-plane and out-of-plane orientation is observed for these films, as shown in figure 8. The (102) GdBCO pole figure shows a 4-fold symmetry and sharp peaks indicating fully epitaxial growth with cube-on-cube relation-ship. The FWHM values of (102)GdBCO, $\Delta\phi$, as well as of the (005)GdBCO rocking curve, $\Delta\omega$, are around 1.12° and 0.34°, respectively (figures 8(a) and (b), respectively), comparable to the values obtained for films prepared by physical methods indicating the high-quality of our films [55].

The microstructure of the optimized films was checked by SEM on their cross-sections and is shown in figure 9. After the pyrolysis, homogeneous films of 400 nm thickness with very smooth surfaces are obtained, figure 9(a). After the complete growth process (figure 9(b)), the films are approximately 220 nm thick and very homogenous and dense
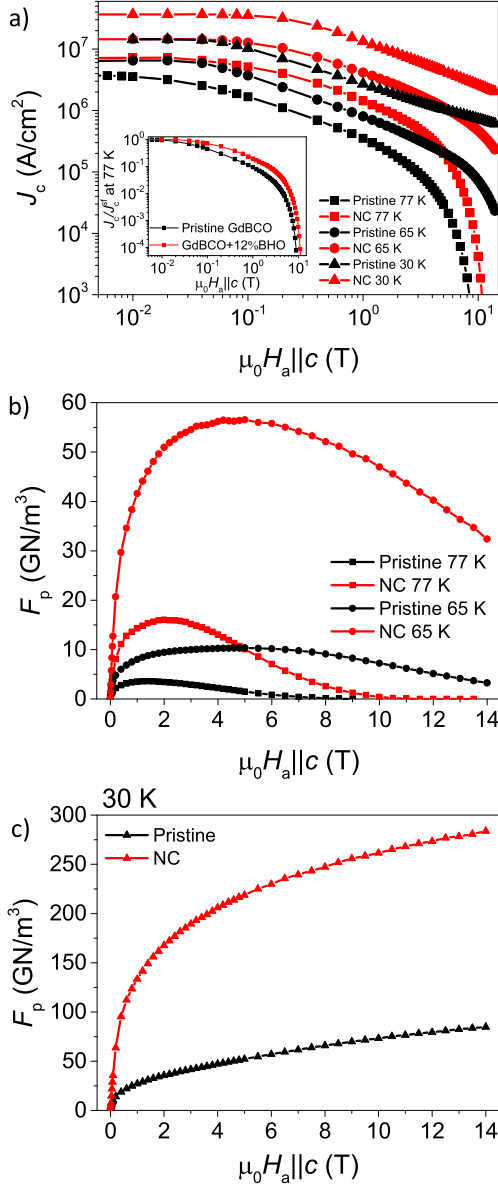
Figure 10. Transport measurements on an optimized GdBCO + 12%BHO film (NC in the legend, red curves) in comparison with a pristine GdBCO film (black curves) showing (a) the J_c dependence with the magnetic field at 77 K (squares), 65 K (circles) and 30 K (triangles), (b) pinning force density (F_p) at 77 K (squares) and 65 K (circles) and (c) F_p at 30 K.

with nearly no pores, which is in accordance with the observations in the top-view SEM images, figure 5. The BHO NPs, marked with blue arrows in figure 9(c), are homogeneously distributed within the film and have a size of 15–20 nm. These results are similar to the previous work published by our group [36].

Figure 10 illustrates the strong improvement in $J_c(H)$ (a) and $F_p(H)$ (b) for all magnetic fields at several temperatures, 77, 65 and 30 K of an optimized GdBCO + 12%BHO NC (red curves) in comparison with a pristine GdBCO film (black curves). The in-field improvement is also clearly seen in the inset, showing the normalized field dependence, $J_c(H)/J_c^{sf}$, at
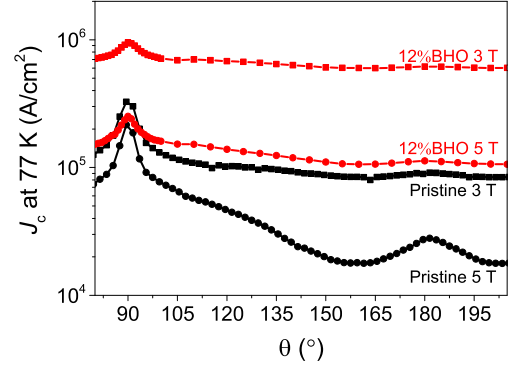
Figure 11. $J_c(\theta)$ at 3 T and 5 T and 77 K for a GdBCO + 12%BHO film (red curves) in comparison with a pristine GdBCO film (black curves).

77 K. The large values of J_c^{sf} that were obtained are noteworthy: 7.3 MA cm^{-2} at 77 K, 14.5 MA cm^{-2} at 65 K and 36.8 MA cm^{-2} at 30 K. These values are the highest ever reported for CSD-grown GdBCO films and among the highest for *RE*BCO films. The excellent in-plane and out-of-plane texture, the absence of impurity phases, the high density with nearly no pores and the homogeneous distribution of NPs within the films are the origin of such high values of J_c^{sf}. Close values were reported for YBCO + 10%BZO films with similar thickness to the films presented in this work [34, 35].

We also obtained large maximum F_p values, F_{pmax}, at the measurement temperatures: 16.0 GN m^{-3} (2 T) at 77 K and 56.5 GN m^{-3} (5 T) at 65 K, which are also the highest ever reported for CSD-grown GdBCO films and among the highest in the literature for CSD-grown *RE*BCO films. Only the above mentioned YBCO + 10%BZO films report similar values [34, 35]. By the use of a physical growth techniques, PLD, slightly higher F_p values were reported for GdBCO films with BHO [44, 56] and BaSnO$_3$ [57] nanocolumns but only for $B||c$, i.e. on cost of anisotropy.

As can be seen in figure 11 showing the angular dependence of J_c with regard to sample orientation, $J_c(\theta)$, for two magnetic fields at 77 K, J_c is increased in the whole angular range by the addition of BHO NPs. Furthermore, the J_c anisotropy ratio, $J_c(H//ab)/J_c(H//c)$ is decreased considerably in the GdBCO + 12%BHO NC. For instance, at 3 T the ratio observed in our pristine GdBCO film is ~3.6 whereas in the NCs it is only ~1.5.

The anisotropic behavior of the NC films can be characterized by a field-independent anisotropy parameter, γ_J, when the anisotropic Ginzburg Landau scaling behavior of $J_c(\theta, H)$ at fixed temperatures is studied. As proposed by Blatter *et al* [58] and first applied to *RE*BCO films by Xu *et al* [59], the isotropic and anisotropic contributions to $J_c(\theta, H)$ can be extracted from a plot of the effective field $H_{eff} = \varepsilon(\theta)H$, where $\varepsilon(\theta) = [\cos^2(\theta) + \gamma^{-2}\sin^2(\theta)]^{1/2}$ and γ is the mass anisotropy ratio [60]. In the case of the GdBCO + 12%BHO NC films studied here, it is concluded that scaling can only be achieved with an effective γ_J value of ~1.6 instead of the expected $\gamma_J \sim 5$–7 value for pristine *RE*BCO films. For this reduction in γ_J by the addition of NPs,
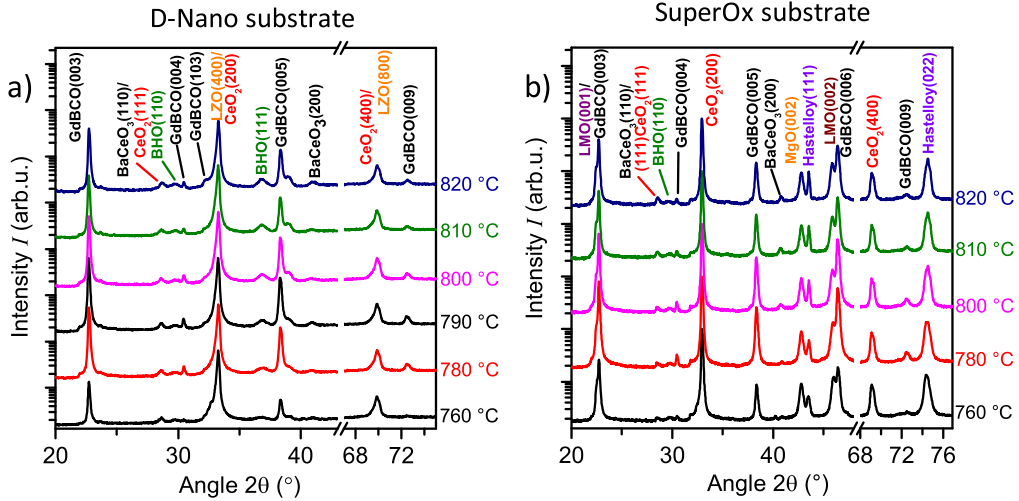
Figure 12. Growth temperature dependence of the XRD patterns of GdBCO + 12%BHO films grown on (a) Deutsche Nanoschicht GmbH (D Nano) tapes and (b) SuperOx tapes.
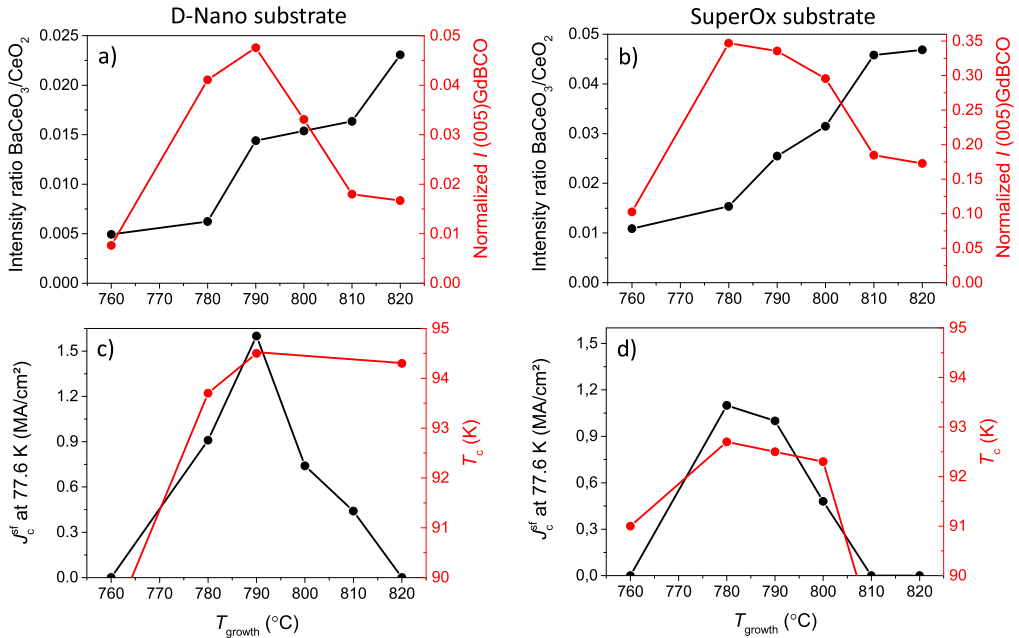
Figure 13. Evolution of the (200)BCO/(200)CeO$_2$ peaks intensity ratio and intensity of (005)GdBCO reflection with the growth temperature for GdBCO + 12%BHO films deposited on (a) D Nano tape and (b) SuperOx tape and the evolution of J_c^{sf} at 77.6 K and T_c with growth temperature for GdBCO + 12%BHO films deposited on (c) D Nano tape and (d) SuperOx tape. Lines are guide for the eyes.

several explanations can be found in literature which all might contribute to some extend: geometrical effects for sufficiently small particles [61], dirty-limit scattering and a change in coherence length anisotropy (discussed especially for PLD-grown films) [62] and a change in the pairing mechanism due to strain fields around the NPs (especially in CSD-grown films) [34, 35].

The *ab*-peak at 90° of the NC film is broadened compared to pristine films. This is attributed to the higher density of short stacking faults that are effective pinning centers for fields nearly parallel to the *a b* plane as observed previously in other CSD NC films [34, 37].

3.3. NC films on buffered metallic tapes

Due to the excellent superconducting properties of GdBCO + 12%BHO obtained on STO, the deposition parameters were transferred to the system of tapes. Tapes supplied by two different companies (Deutsche Nanoschicht GmbH (D-Nano) and SuperOx) with different layer architectures were studied. The D-Nano tape is a fully CSD-buffered RABiTS tape consisting of a top thin layer of CeO$_2$ on three layers of ~100 nm La$_2$Zr$_2$O$_7$ (LZO) that are, in turn, deposited on top of a biaxially textured Ni-W alloy substrate (CeO$_{2CSD}$/LZO$_{CSD}$/Ni-W$_{RABiTS}$) [63]. The SuperOx tape is an IBAD-based substrate with the following stacking
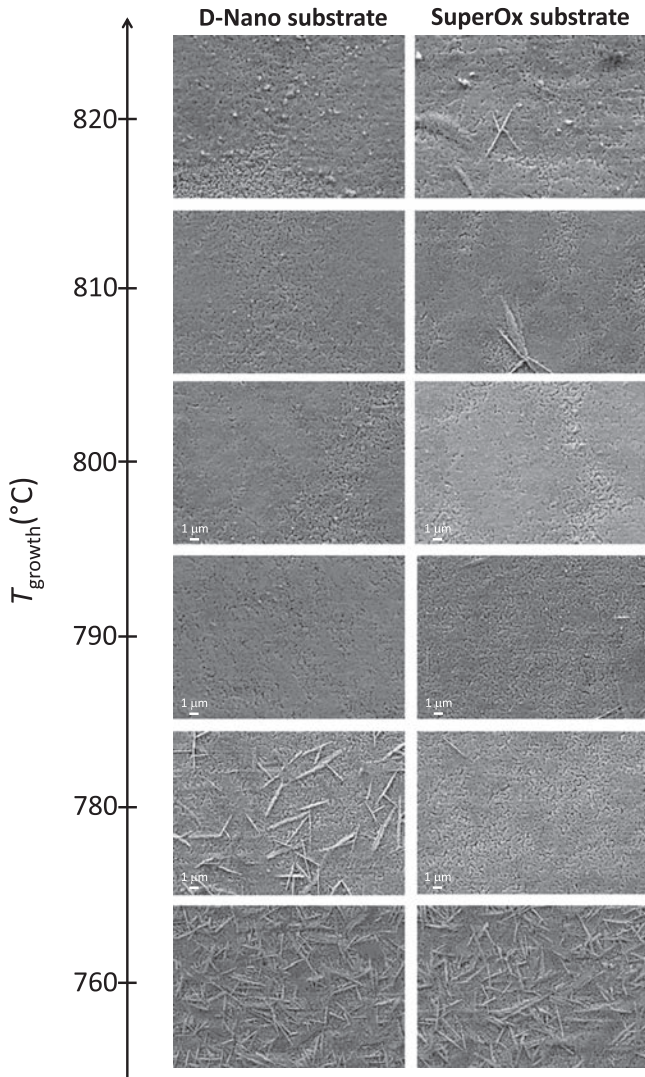
Figure 14. SEM top view images of GdBCO + 12%BHO films deposited on the two different tapes and grown at different temperatures.

sequence: PLD-grown 100–200 nm thick CeO_2 on a magnetron-sputtered 30–50 nm $LaMnO_3$ (LMO) on 5–7 nm IBAD-MgO on 30–50 nm Y_2O_3 or LMO and 50 nm Al_2O_3 deposited on a $\sim 60\,\mu$m thick non-magnetic Hastelloy C276 substrate (CeO_2/LMO/IBAD-MgO/Y_2O_3(LMO)/Al_2O_3/Hastelloy C276) [41]. For the film growth on tapes, we used the optimized heating ramp (85 °C min^{-1}) and oxygen partial pressure (50 ppm) obtained on STO. However, the crystallization temperature should in general be lower on tapes than on single crystals in order to avoid structural instabilities induced at too high temperatures due to the different heat conduction and capacity properties. Therefore, T_{growth} has been scanned again.

The XRD patterns of the two temperature series, figure 12, show that a high degree of (00l) texture of GdBCO is achieved on both tapes in the whole temperature range studied. Only some traces of misoriented grains, characterized by the presence of (103)GdBCO and (h00)GdBCO is detected at the lowest growth temperature of 760 °C on both tapes. The BHO NPs are also formed on tapes as evidenced by the BHO-related reflections. Moreover, for all growth temperatures $BaCeO_3$ (BCO) peaks appear in the diffractograms. This points to reactivity between the GdBCO precursors and the CeO_2 layer during the GdBCO formation reaction, a phenomenon previously reported for YBCO growth on RABiTS tapes [64]. Most likely, the BaF_2 that is generated during the intermediate reactions reacts with CeO_2 to form BCO. The formation of BCO takes place at the CeO_2/GdBCO interface and hinders the epitaxial growth of GdBCO, if BCO is formed prior to the nucleation of GdBCO. In that case GdBCO has to grow on top of BCO, and since BCO has a large mismatch to GdBCO, unlike CeO_2, this contributes to the generation of GdBCO misoriented grains. On the other hand, if the heteroepitaxial nucleation of GdBCO at the CeO_2 layer occurs before the BCO formation, the BCO generation is not as severe, because large areas of the interface are covered with the GdBCO nuclei and BCO does not disturb the epitaxial growth of GdBCO. Our system tends towards the second case because no misoriented grains are visible except for 760 °C and the intensities of BCO reflections are quite low.

Nevertheless, it is always preferable to avoid this reactivity entirely by choosing the most appropriate growth conditions. The ratio

$$\frac{I(200)\,BCO}{I(200)\,CeO_2 + I(200)\,BCO}$$

is a measure for the amount of BCO formed for a certain CeO_2 layer thickness. These two peaks were chosen because for BCO the (200) peak varies the most with temperature and for CeO_2 the (200) peak is the most intense one. For the D-Nano tapes, (200)CeO_2 coincides with (400)LZO, so the measured intensity comes from both phases. However, we assume that the possible changes in intensity only come from variations in the CeO_2 film while the LZO remains stable for the temperatures studied here and, therefore, the ratio is still meaningful. Additionally, the intensity of the (005)GdBCO reflection (normalized to the most intense peak of the temperature-stable templates, i.e. the Ni-W for D-Nano and (002)CeO_2 for SuperOx) reveals the growth temperature dependence of the c-axis texture quality.

As the (200)BCO/(200)CeO_2 ratio in figure 13 indicates, the interface reactivity increases for both tapes with temperature similarly strong (factor 4 between 760 °C and 820 °C). Regarding reactivity, the optimum growth temperature would therefore be the lowest. However, the (005)GdBCO peak intensity shows a different behavior. It reaches a maximum value at medium temperatures around 780 °C–790 °C. As demonstrated in the previous sections, the epitaxial growth of the GdBCO is not favored at low temperatures. On the other hand, high temperatures (>790 °C) deteriorate the buffer layer surfaces and lead to enhanced BCO formation which affects the GdBCO growth. Therefore, an optimum growth temperature of around 780 °C–790 °C is found, which reflects
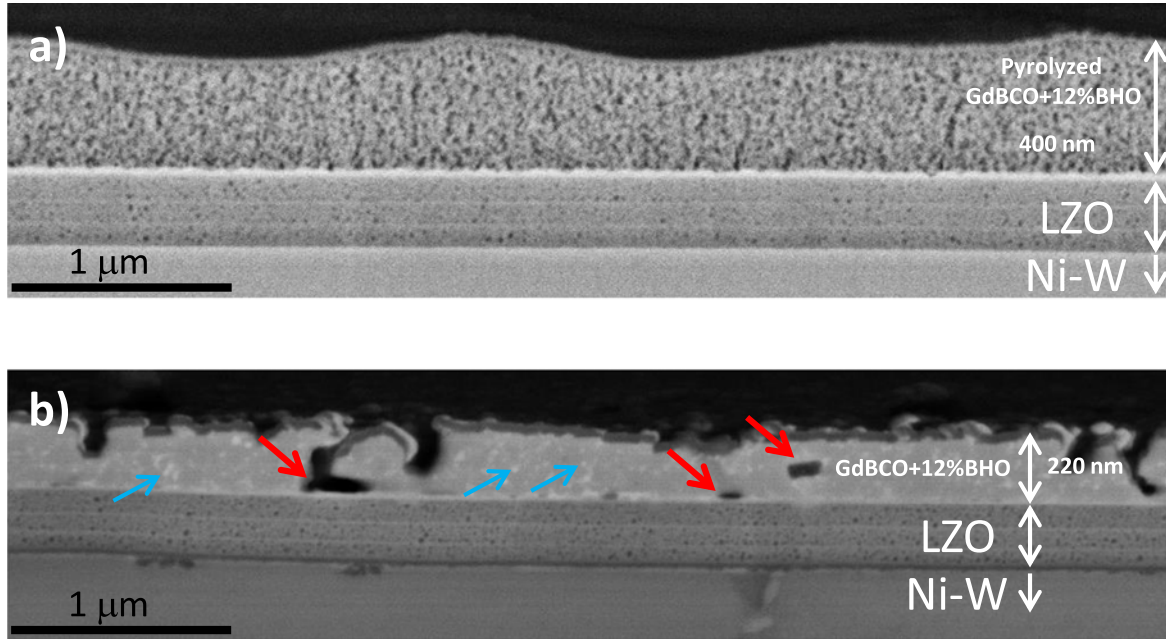
Figure 15. Cross section SEM images on backscattered mode of (a) a pyrolyzed GdBCO + 12%BHO film and (b) a grown GdBCO + 12% BHO film (790 °C, 50 ppm) both deposited on D Nano tapes.

nicely in the growth temperature dependence of the inductive J_c^{sf} at 77.6 K, figure 13. The results achieved, especially on D-Nano substrate, with $T_c = 94.5$ K (even slightly higher than optimized on STO) and J_c^{sf} at 77.6 K = 1.6 MA cm^{-2}, are the highest in the literature for CSD GdBCO-based films on tapes. The values of the films on SuperOx tape are comparable to the D-Nano tapes at the same processing conditions, yet with 1.1 MA cm^{-2} and 92.7 K somewhat lower.

Although the superconducting properties of the GdBCO + 12%BHO NCs deposited on tapes are promising, the J_c values are still far below the values achieved on STO. This is partially due to the grain-boundary networks in the films on tape [65]. Besides that, other defects strongly contribute to the J_c reduction, as seen in figures 14 and 15. Figure 14 depicts SEM images of the surface morphology of different GdBCO + 12%BHO films grown at different temperatures on both tapes. In general, the films present a high degree of porosity whereas the films around 790 °C show the most homogeneous surfaces, well corresponding to the maxima in (005)GdBCO intensity and J_c. At lower growth temperatures, the density of pores is higher and the films contain a large amount of misoriented grains. At higher temperatures, the formation of misoriented grains can be avoided but the porosity is still present. As it is well-known, the porosity can be reduced by increasing the temperature favouring sintering processes. However, on tapes the increase in temperature causes the opposite effect. For both tapes, porosity as well as inhomogeneities are strongly increased. This is attributed to the fact that at high temperatures the buffer layer surfaces of the tapes start to lose the structural integrity degrading the growth of GdBCO and causing these highly porous areas.

As discussed in detail in [30] and [47], the presence of porosity strongly degrades J_c. The pores reduce the cross-section and hinder the current flow. Cross-sectional SEM images in figure 15 show a pyrolyzed film and a film grown at optimum temperature (790 °C). The only-pyrolyzed film is macroscopically homogeneous in its volume (400 nm thick), however, with a much larger thickness variation than films on STO. It contains a large number of small pores which is typical for CSD films after the pyrolysis step as observed previously in YBCO films deposited on single crystals [66]. On the other hand, the crystallized films (220 nm thick) contain large pores and trenches (red arrows), in some cases even extending all the way from the interface to the film surface. This is in contrast to the STO case in which the films present a very dense microstructure without any pores. For further enhancement of J_c on tapes in follow-up studies the pores and trenches have to be avoided, most likely by minimizing the thickness variation of the pyrolyzed films by additionally scanning heating rate and oxygen partial pressure and other parameters again. The BHO NPs (blue arrows in figure 15(b), however, show very homogenous size and density distributions throughout the film thickness leading to the good superconducting properties ($T_c = 94.5$ K and J_c^{sf} at 77.6 K = 1.6 MA cm^{-2}). The high T_c with a small transition width of 1 K indicates high phase homogeneity. Therefore, by reducing the porosity of the films it should be possible to obtain much higher J_c values in future. The fact that keeping the structural integrity of the buffer interface calls for lower crystallization temperatures for GdBCO film growth than actually required makes it necessary to look for alternative approaches. One way might be the acceleration of the growth in order to inhibit the reaction with the interface. With that, it should be possible to obtain epitaxial GdBCO films at

standard GdBCO temperatures and therefore with reduced porosity.

4. Conclusions

We have studied the influence of different processing parameters in the growth of GdBCO + 12%BHO films deposited on STO single crystals and on tapes. The operation window for achieving good superconducting properties in this kind of films is very narrow on both types of substrates. The optimum conditions we found for the growth on STO are a heating ramp of 85 °C min^{-1}, a crystallization temperature T_{growth} of 810 °C and an oxygen partial pressure $p(\text{O}_2)$ of 50 ppm. Under these conditions, excellent fully epitaxial superconducting films are achieved and large values of J_c^{sf} (7.3 MA cm^{-2} at 77 K, 14.5 MA cm^{-2} at 65 K and 36.8 MA cm^{-2} at 30 K) and F_{pmax} (16.0 GN m^{-3} at 77 K and 2 T as well 56.5 GN m^{-3} at 65 K and 5 T) are reached being among the highest ever reported for CSD REBCO films. The growth on tapes is more challenging due to their limitations to avoid buffer degradation. Despite this, we have obtained films that present promising superconducting properties and that open the possibility for further optimization to finally achieve values closer to those on single crystals.

Acknowledgments

References

[1] Iijima Y *et al* 1991 Biaxially aligned YBa$_2$Cu$_3$O$_{7-x}$ thin film tapes *Phys. C Supercond.* **185 189** 1959 60
[2] Hasegawa K *et al* 1996 Biaxially aligned YBCO film tapes fabricated by all pulsed laser deposition *Appl. Supercond.* **4** 487 93
[3] Goyal A *et al* 2004 The RABiTS approach: using rolling assisted biaxially textured substrates for high performance YBCO superconductors *MRS Bull.* **29** 552 61
[4] Balachandran U *et al* 1994 Recent advances in bismuth based superconductors *JOM* **46** 23 5
[5] Malozemoff A P *et al* 1999 HTS wire at commercial performance levels *IEEE Trans. Appl. Supercond.* **9** 2469 73
[6] Scanlan R M *et al* 2004 Superconducting materials for large scale applications *Proc. IEEE* **92** 1639 54
[7] Murakami M *et al* 1996 Melt processed light rare earth element Ba Cu O *Supercond. Sci. Technol.* **9** 1015 32
[8] Yoshida Y *et al* 2008 Progress in development of advanced PLD process for high J_c REBCO film *Phys. C Supercond.* **468** 1606 10
[9] Wee S H *et al* 2006 High in field critical current densities in epitaxial NdBa$_2$Cu$_3$O$_{7-\delta}$ films on RABiTS by pulsed laser deposition *Supercond. Sci. Technol.* **19** 865 8
[10] Andreouli C and Tsetsekou A 1997 Synthesis of HTSC Re(Y)Ba$_2$Cu$_3$O$_x$ powders: the role of ionic radius *Phys. C Supercond.* **291** 274 86
[11] MacManus Driscoll J L *et al* 1994 Studies of structural disorder in ReBa$_2$Cu$_3$O$_{7-x}$ thin films (Re = rare earth) as a function of rare earth ionic radius and film deposition conditions *Phys. C Supercond.* **232** 288 308
[12] MacManus Driscoll J L *et al* 2004 Systematic enhancement of in field critical current density with rare earth ion size variance in superconducting rare earth barium cuprate films *Appl. Phys. Lett.* **84** 5329 31
[13] MacManus Driscoll J L *et al* 2005 Rare earth ion size effects and enhanced critical current densities in Y$_{2/3}$Sm$_{1/3}$Ba$_2$Cu$_3$O$_{7-x}$ coated conductors *Appl. Phys. Lett.* **86** 32505
[14] Islam M S and Baetzold R C 1989 Atomistic simulation of dopant substitution in YBa$_2$Cu$_3$O$_7$ *Phys. Rev.* B **40** 10926 35
[15] Macmanus Driscoll J L 1997 Materials chemistry and thermodynamics of REBa$_2$Cu$_3$O$_{7-x}$ *Adv. Mater.* **9** 457 73
[16] Iye Y *et al* 1987 Critical field anisotropy of a single crystal GdBa$_2$Cu$_3$O$_x$ and HoBa$_2$Cu$_3$O$_x$ *Japan. J. Appl. Phys.* **26** L1850 2
[17] Iguchi T *et al* 2002 Fabrication of GdBaCuO films by the metal organic deposition method using trifluoroacetates *Supercond. Sci. Technol.* **15** 1415 20
[18] Andrä W *et al* 1991 Rotational hysteresis losses in sputtered rebco films of different structure *Phys. C Supercond.* **185 189** 2169 70
[19] Luo Q *et al* 2014 Effect of the O$_2$/Ar pressure ratio on the microstructure and surface morphology of Epi MgO/IBAD MgO templates for GdBa$_2$Cu$_3$O$_{7-\delta}$ coated conductors *Chin. Phys. Lett.* **31** 37402
[20] Wang Y *et al* 2013 Dependencies of microstructure and stress on the thickness of GdBa$_2$Cu$_3$O$_{7-\delta}$ thin films fabricated by RF sputtering *Nanoscale Res. Lett.* **8** 304
[21] Lee S *et al* 2009 Development of in plume pulsed laser deposition of high I_c GdBCO films for coated conductors *IEEE Trans. Appl. Supercond.* **19** 3192 5
[22] Li W *et al* 2014 Fabrication of GdBa$_2$Cu$_3$O$_{7-\delta}$ films by photo assisted MOCVD process *Phys. C Supercond.* **501** 1 6
[23] Obradors X and Puig T 2014 Coated conductors for power applications: materials challenges *Supercond. Sci. Technol.* **27** 44003
[24] Obradors X *et al* 2004 Chemical solution deposition: a path towards low cost coated conductors *Supercond. Sci. Technol.* **17** 1055 64
[25] Obradors X *et al* 2006 Progress towards all chemical superconducting YBa$_2$Cu$_3$O$_7$ coated conductors *Supercond. Sci. Technol.* **19** S13 26
[26] Izumi T *et al* 2007 Progress in development of advanced TFA MOD process for coated conductors *Phys. C Supercond. Appl.* **463** 510 4

[27] Gupta A *et al* 1988 Superconducting oxide films with high transition temperature prepared from metal trifluoroacetate precursors *Appl. Phys. Lett.* **52** 2077 9

[28] Jin L H *et al* 2011 Fabrication of GdBa$_2$Cu$_3$O$_{7-x}$ films by TFA MOD process *J. Alloys Compd.* **509** 3353 6

[29] Kaneko A *et al* 2004 Fabrication of REBa$_2$Cu$_3$O$_{7-y}$ film by advanced TFA MOD process *Phys. C Supercond.* **412** 926 30

[30] Erbe M *et al* 2014 Improved REBa$_2$Cu$_3$O$_{7-x}$ (RE = Y, Gd) structure and superconducting properties by addition of acetylacetone in TFA MOD precursor solutions *J. Mater. Chem. A* **2** 4932

[31] Liu L *et al* 2017 Influence of chemical doping on flux pinning of GdBa$_2$Cu$_3$O$_{7-z}$ films *Surf. Eng.* 1 6

[32] Jin L H *et al* 2013 Development of modified TFA MOD approach for GdBa$_2$Cu$_3$O$_y$ film growth *Mater. Lett.* **94** 23 6

[33] Suzuki H *et al* 2015 Effects of holmium doping on the critical current density in GdBa$_2$Cu$_3$O$_y$ films fabricated by metal organic deposition using fluorine free solutions *Phys. Proc.* **65** 133 6

[34] Gutiérrez J *et al* 2007 Strong isotropic flux pinning in solution derived YBa$_2$Cu$_3$O$_{7-x}$ nanocomposite superconductor films *Nat. Mater.* **6** 367 73

[35] Llordés A *et al* 2012 Nanoscale strain induced pair suppression as a vortex pinning mechanism in high temperature superconductors *Nat. Mater.* **11** 329 36

[36] Erbe M *et al* 2015 BaHfO$_3$ artificial pinning centres in TFA MOD derived YBCO and GdBCO thin films *Supercond. Sci. Technol.* **28** 114002

[37] Cayado P *et al* 2015 Epitaxial YBa$_2$Cu$_3$O$_{7-x}$ nanocomposite thin films from colloidal solutions *Supercond. Sci. Technol.* **28**

[38] De Keukeleere K *et al* 2016 Superconducting YBa$_2$Cu$_3$O$_{7-\delta}$ nanocomposites using preformed ZrO$_2$ nanocrystals: growth mechanisms and vortex pinning properties *Adv. Electron. Mater.* 1600161

[39] Engel S *et al* 2007 Enhanced flux pinning in YBa$_2$Cu$_3$O$_7$ layers by the formation of nanosized BaHfO$_3$ precipitates using the chemical deposition method *Appl. Phys. Lett.* **90** 102505

[40] MacManus Driscoll J L *et al* 2014 Strong pinning in very fast grown reactive co evaporated GdBa$_2$Cu$_3$O$_7$ coated conductors *APL Mater.* **2** 86103

[41] Lee J H *et al* 2014 RCE DR, a novel process for coated conductor fabrication with high performance *Supercond. Sci. Technol.* **27** 44018

[42] Soon Mi Choi *et al* 2013 Characteristics of High J_c GdBCO coated conductors fabricated by the RCE DR process *IEEE Trans. Appl. Supercond.* **23** 8001004

[43] Lao M *et al* 2015 Critical current anisotropy of GdBCO tapes grown on ISD MgO buffered substrate *Supercond. Sci. Technol.* **28** 124002

[44] Awaji S *et al* 2015 High performance irreversibility field and flux pinning force density in BaHfO$_3$ doped GdBa$_2$Cu$_3$O$_y$ tape prepared by pulsed laser deposition *Appl. Phys. Express* **8** 23101

[45] Takahashi K *et al* 2006 Investigation of thick PLD GdBCO and ZrO$_2$ doped GdBCO coated conductors with high critical current on PLD CeO$_2$ capped IBAD GZO substrate tapes *Supercond. Sci. Technol.* **19** 924 9

[46] Ibi A *et al* 2006 Development of long GdBCO coated conductor using the IBAD/MPMT PLD method *Supercond. Sci. Technol.* **19** 1229 32

[47] Zalamova K *et al* 2006 Smooth stress relief of trifluoroacetate metal organic solutions for YBa$_2$Cu$_3$O$_7$ film growth *Chem. Mater.* **18** 5897 906

[48] Cayado P 2016 Multifunctional nanostructured superconductors by chemical routes: towards high current conductors *PhD Thesis* ICMAB C 2, pp 41 50

[49] Lee J W *et al* 2014 Stability phase diagram of GdBa$_2$Cu$_3$O$_{7-\delta}$ in low oxygen pressures *J. Alloys Compd.* **602** 78 86

[50] Taïr F *et al* 2017 Melting temperature of YBa$_2$Cu$_3$O$_{7-x}$ and GdBa$_2$Cu$_3$O$_{7-x}$ at subatmospheric partial pressure *J. Alloys Compd.* **692** 787 92

[51] Feenstra R *et al* 1991 Effect of oxygen pressure on the synthesis of YBa$_2$Cu$_3$O$_{7-x}$ thin films by post deposition annealing *J. Appl. Phys.* **69** 6569 85

[52] Jooss C *et al* 2002 Magneto optical studies of current distributions in high T_c superconductors *Rep. Prog. Phys.* **65** 651 788

[53] Koblischka M R and Wijngaarden R J 1995 Magneto optical investigations of superconductors *Supercond. Sci. Technol.* **8** 199 213

[54] Mikheenko P *et al* 2012 Magneto optical imaging of columnar YBCO films *Phys. Proc.* **36** 623 8

[55] Rosenzweig S *et al* 2010 Irreversibility field up to 42 T of GdBa$_2$Cu$_3$O$_{7-\delta}$ thin films grown by PLD and its dependence on deposition parameters *Supercond. Sci. Technol.* **23** 105017

[56] Hikawa K *et al* 2014 Influence of Gd/Ba composition on superconducting properties of BaHfO$_3$ doped Gd$_{1+x}$Ba$_{2-x}$Cu$_3$O$_y$ films *Phys. Proc.* **58** 158 61

[57] Ko K P *et al* 2011 Strongly enhanced flux pining of GdBCO coated conductors with BaSnO$_3$ nanorods by pulsed laser deposition *Phys. C Supercond. Appl.* **471** 940 3

[58] Blatter G *et al* 1992 From isotropic to anisotropic superconductors: a scaling approach *Phys. Rev. Lett.* **68** 875 8

[59] Xu X *et al* 1994 Angular dependence of the critical current density for epitaxial YBa$_2$Cu$_3$O$_{7-\sigma}$ thin film *Solid State Commun.* **92** 501 4

[60] Civale L *et al* 2004 Understanding high critical currents in YBa$_2$Cu$_3$O$_7$ thin films and coated conductors *J. Low Temp. Phys.* **135** 87 98

[61] van der Beek C J *et al* 2012 Anisotropy of strong pinning in multi band superconductors *Supercond. Sci. Technol.* **25** 84010

[62] Malmivirta M *et al* 2016 Dirty limit scattering behind the decreased anisotropy of doped YBa$_2$Cu$_3$O$_{7-\delta}$ thin films *J. Phys. Condens. Matter* **28** 175702

[63] Witte M *et al* 2014 The project SupraMetall: towards commercial fabrication of high temperature superconducting tapes *Adv. Eng. Mater.* **16** 539 49

[64] Parans Paranthaman M *et al* 2006 All MOD buffer/YBCO approach to coated conductors *Phys. C Supercond.* **445 448** 529 32

[65] Feldmann D M *et al* 2007 Mechanisms for enhanced supercurrent across meandered grain boundaries in high temperature superconductors *J. Appl. Phys.* **102** 83912

[66] Palmer X *et al* 2016 Solution design for low fluorine trifluoroacetate route to YBa$_2$Cu$_3$O$_7$ films *Supercond. Sci. Technol.* **29** 24002

Repository KITopen